Acta Materialia 306 (2026) 121909

Contents lists available at ScienceDirect

Acta Materialia

journal homepage: www.elsevier.com/locate/actamat

Heterogeneous-phase-mediated plastic deformation and phase transformation of titanium upon deviatoric stress

Bo Li [a,b,*], Chenhui Hu [a], Kaiyuan Shi [c], Lei Su [c,d,*], Yizhe Cao [a], Huiying Liu [a], Dongxu Hui [a], Shaodi Wang [a], Chuanwei Fan [e], Katsuyoshi Kondoh [f], Xin Zhang [a,b], Shengyin Zhou [a,b], Shufeng Li [a,b,*]

[a] School of Materials Science and Engineering, Xi'an University of Technology, Xi'an 710048, China
[b] Xi'an Key Laboratory of Advanced Powder Metallurgy Materials and New Technology, Xi'an University of Technology, Xi'an 710048, China
[c] Center for High Pressure Science and Technology Advanced Research (HPSTAR), Beijing 100093, China
[d] Shanghai Advanced Research in Physical Sciences (SHARPS), Shanghai 201203, China
[e] State Key Laboratory for Mechanical Behavior of Materials, School of Materials Science and Engineering, Xi'an Jiaotong University, Xi'an 710049, China
[f] Joining and Welding Research Institute, Osaka University, Ibaraki, Osaka 567-0047, Japan

ARTICLE INFO

Keywords:
Titanium
Heterogeneity
Phase transformation
Dislocation density
Synchrotron diffraction

ABSTRACT

Deviatoric stress and microstructural imperfections are considered the main reasons for the promotion of phase transformation (PT) of metals at high pressure. However, structural heterogeneity induced by secondary phases will pose challenges for understanding the high-pressure deformation and PT of metallic composites. For instance, anomalies related to kinetic suppression were observed in the forward (α→ω) and reverse (ω→α) transformation of α-Ti confined by TiB upon nonhydrostatic pressure. Here, static/dynamic diamond anvil cells and synchrotron X-ray diffraction were utilized to panoramically resolve the dislocation evolution in plastic flow deformation and strain-induced PT of Ti-TiB microcomposite. Diffraction peak profile analysis reveals a decrease in dislocation density of confined α-Ti from plastic flow (1×10^{16} m^{-2}) to strain-induced PT (6.7×10^{15} m^{-2}), accompanied with the activation of ~60% <a> slip systems and a varying combination of <c> and <c+a>. Long-range internal stress at Ti/TiB interface increases quasi-linearly to a maximum accounting for ~17% of total pressure as the nonhydrostatic pressure increases. It probably indicates the key role of heterogeneous-stress-partition in lowering local stress required for the dislocation-mediated growth of critical ω nucleus. Furthermore, analytical results demonstrate the kinetics of PT of Ti and Ti-TiB could be well unified through the Levitas's strain-induced kinetic equation, though their accumulated plastic strain differs by a factor of ~3. This work shed light on the role of heterogeneous phase in high-pressure deformation and PT of metals and display promising applications such as manipulation of pressure-related strength/plasticity and PT kinetics of metals via compatible second-phases.

1. Introduction

Pressure-driven phase transformation (PT) is common in a wide range of structural and functional applications of hexagonal close-packed (HCP) metals, such as Ti, Zr and Hf [1–3]. At room temperature, ambient stable α-Ti could transform to metastable ω phase (hexagonal) during martensitic transformation induced by extreme loadings, e.g., diamond anvil cells (DAC) [4,5], high-pressure torsion [6], impact and shockwave loading [7–9]. For practical applications, however, it is unfortunate that the simple hexagonal ω phase lowers the toughness and ductility, and becomes anisotropic compared to parent α phase [10,11]. Thus, the transition pathway and kinetics of Ti during forward (α→ω) and reverse (ω→α) transformations have been broadly investigated [11–13]. Experimentally, a direct transformation pathway identified by the orientation relationships (ORs) between α and ω phases, specifically, $(00.1)_\alpha \parallel (11.0)_\omega$, $[11.0]_\alpha \parallel [00.1]_\omega$, was first proposed by Silcock [14]. Later, Trinkle et al. proposed the TAO-1 pathway via ab-initio calculations, that is, the lowest energy pathway following the ORs of $(00.1)_\alpha \parallel (0\bar{1}1)_\omega$, $[11.0]_\alpha \parallel [01.1]_\omega$ [12]. Although two pathways have been widely accepted, the kinetics of α→ω PT of Ti is still an open question

* Corresponding authors.
E-mail addresses: libo930@xaut.edu.cn (B. Li), lei.su@sharps.ac.cn (L. Su), shufengli@xaut.edu.cn (S. Li).

https://doi.org/10.1016/j.actamat.2026.121909
Received 25 September 2025; Received in revised form 16 December 2025; Accepted 8 January 2026
Available online 11 January 2026
1359-6454/

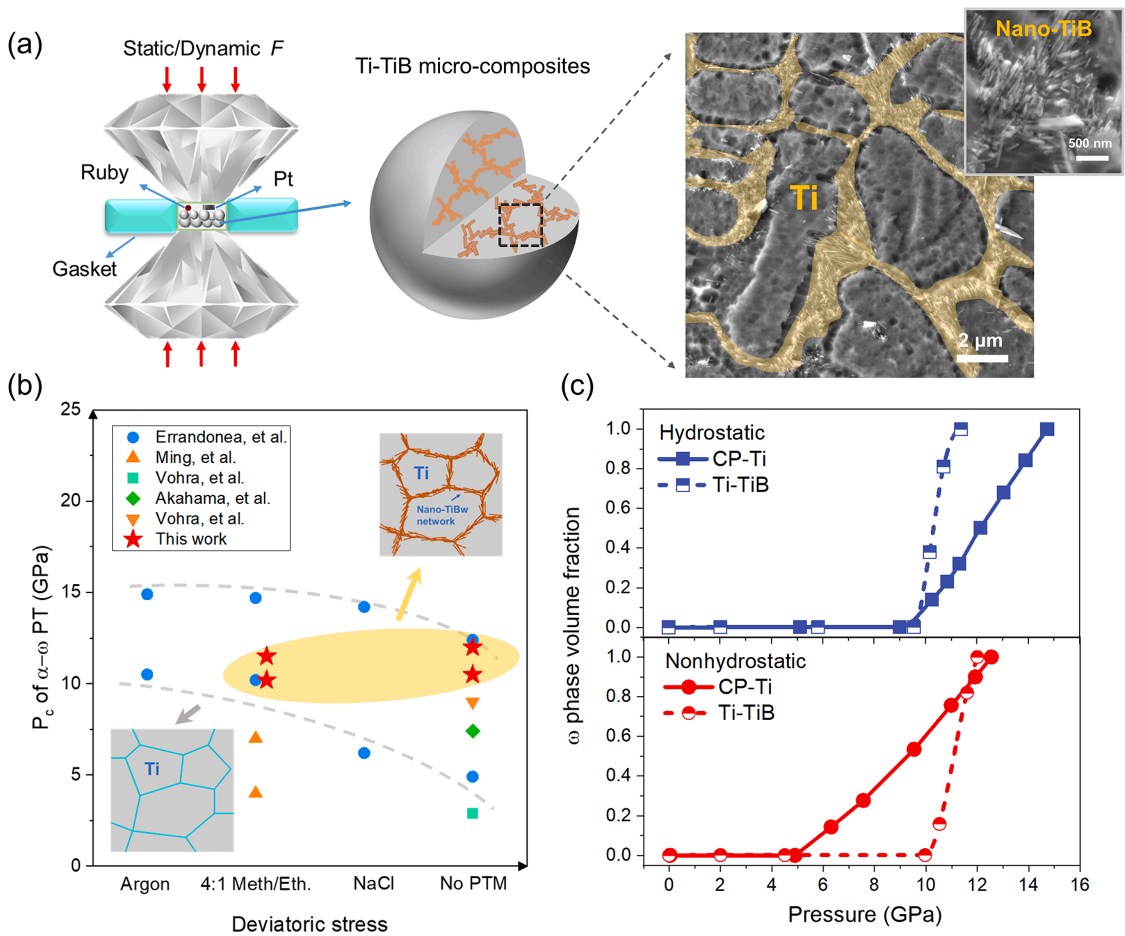

Fig. 1. High-pressure PT anomaly observed in α-Ti confined by TiB network. (a) Static/dynamic DAC apparatus and microstructure of Ti-TiB microcomposite. The network consisting of TiB nanowhiskers are highlighted and magnified as shown in SEM images. (b) Critical pressure of α→ω transformation in Ti-TiB (stars) and CP-Ti (dots) under hydrostatic and nonhydrostatic conditions. Dashed lines indicate the lower and upper pressure bounds of α→ω transformation for CP-Ti. (c) The volume fraction of ω phase in Ti-TiB and CP-Ti as a function of pressure.

due to a fact that the critical (onset) pressure falls within a scattered range of 2–10 GPa for quasistatic experiments [4,11–13,15–18]. The deviatoric stress superimposed on hydrostatic pressure, as well as internal impurities or defects are found to be the roots for the promotion of α→ω PT [4,15,16,19]. Even the recovery hysteresis of ω→α PT also depends on the severity of deviatoric stress. The severe plastic strain imposed by deviatoric stress could lead to internal defects that stabilize the ω phase [7,10,20]. As classified by Levitas et al., pressure-induced (hydrostatic) and stress-induced (nonhydrostatic) PT occurs mainly by the nucleation at pre-existing defects below yielding, while strain-induced PT is activated by new defects generated during plastic deformation [2,21]. In particular for strain-induced PT, dislocation-mediated stress from a dislocation pileup against grain boundaries (GBs) could reduce the critical pressure of α→ω PT since the interfacial stress is much larger than average equilibrium stress [22]. Thus, dislocations and their interaction with other factors such as twin/phase/grain boundaries and heterogeneous interfaces are also crucial for the kinetics of PTs [19,23–26]. Theoretical studies by concurrent atomistic-continuum and phase field approaches have already established a clear physical picture of microscale PT mechanism based on dislocation level simulations [27–29]. Compared to extensive studies on the dislocation-GB interactions for the PTs of metals, the dislocation behavior in strain-induced PT for multiphase materials with heterogeneous interfaces, for example, metallic composite, has drawn burgeoning concerns [26].

Compositing via the addition of secondary phases, e.g., particles, whiskers and fibers, will cause lattice distortion, grain refinement, and the increase of dislocation density and microstrain within metals. Therefore, the scenario of PT for a second-phase-reinforced composite becomes far more complicated since the kinetics can be influenced by several variables and their interactions with defects, including volume fraction, geometry, interfacial strength and spatial distribution of secondary phases. For Ti and its alloys, TiB is an ideal reinforcement and has been widely used due to high compatibility of crystallographic and physical properties between both [30]. Taking Ti-TiB composite for example, the strong Zener pinning effect of TiB whiskers has been demonstrated not only to significantly improve the strength and toughness, but to enhance the critical pressure of α→ω PT under nonhydrostatic pressure [30,31]. Peng et al. preformed the atomistic-to-microscale simulation of dislocation pileup-induced internal stress near a heterogenous interface of dual-phase materials and display the potential significance of secondary phases on the strain-induced PT [26].These advances require experimental evidences related to microstructural details to reveal the underlying mechanisms for strain-induced PT of multiphase materials. To this end, it is essential to determine dislocation character, Burgers vector population and dislocation density, to help understand the heterogeneous-phase-mediated constraint effect on plastic deformation and strain-induced PT of metals and rationalize the kinetic equation for multiphase materials at high pressure.

Here, micron-sized Ti-TiB composite was employed as a model material to scrutinize the dislocation evolution of α-Ti confined by TiB nanowhiskers upon nonhydrostatic pressure via the combination of static/dynamic diamond anvil cells and synchrotron X-ray diffraction (SXRD). Diffraction peak profile analysis (DPPA) based on the dislocation model of strain anisotropy was used to panoramically resolve the activated slip systems and dislocation density of Ti-TiB during severe plastic flow and strain-induced α→ω transformation. DPPA of X-ray/neutron diffraction pattern provides a robust way to quantify the coherent domain size, microstrain and dislocation density according to the dislocation model of strain anisotropy for deformed metals by Ungár et al. [32–34]. This methodology expands on dislocation analysis by transmission electron microscopy even on individual grain level and in the cases that are employed sophisticated sample environments such as in-situ deformation at small-length scale and high-pressure diamond cells [35,36]. In addition, the classic Mughrabi's composite model was modified to accommodate the Ti-TiB configuration and the magnitude of heterogeneous constraint in a Ti-TiB cell was estimated in terms of long-range internal stress associated with geometrically necessary dislocations (GNDs). In addition, the influence of TiB constraint on the recovery hysteresis of ω→α PT in Ti-TiB and commercially pure titanium (CP-Ti) under dynamic conditions was also discussed. Finally, the kinetic equation of Ti-TiB regarding to strain-induced PT was established based on Levitas's nanoscale mechanism and the pressure-temperature (P-T) phase diagram of Ti was revisited in terms of heterogeneous effect.

2. Materials and methods

2.1. Fabrication of Ti-TiB microparticles suitable for DAC experiment

The Ti-TiB microparticles were prepared using electrode induced gas atomization (EIGA) and see details in supplementary material. According to Ti-B phase diagram, the content of TiB of our sample is 3.4 vol % (B ~0.57 wt %), which is far less than the eutectic content [30]. As a consequence, the solidification follows: liquid → primary β-Ti + liquid → primary β-Ti + eutectic (TiB + β-Ti) → α-Ti + α''. During the cooling process, the eutectic (TiB + β-Ti) precipitates along primary β-Ti boundaries to form the network structure [37]. Though there might exist solute boron atoms in α-Ti under non-equilibrium process, the trace content can be reasonably negligible. In addition, the diffraction peaks of α and α'' phases are very close at low angle region as shown in Fig. S1. Note that the second strongest peak (02.1) at 41.2° is one of main signatures for α'' phase, which was not detected in our SXRD data. Thus, we will limit our discussion only to the dominant α-Ti.

The scanning electron microscope (SEM) morphology of pristine Ti-TiB microparticles is illustrated in Fig. 1a. The composite particles possess near equiaxed α-Ti grains with an average diameter of ~3 μm. In order to avoid the influence of impurities, we make sure the Ti-TiB particles with a low content of oxygen~1100 and nitrogen~150 ppm, which are lower than CP-Ti (ASTM Grade1). This ensures that possible differences of their high-pressure behaviors can only be ascribed to the pressure environment and microstructure of samples [13,15,16].

2.2. High-pressure experiment and characterization

High pressure experiments were performed using symmetrical DAC with ~300 μm culets. The hydrostatic and nonhydrostatic conditions were realized with the pressure transmitting medium (PTM) of 4:1 methanol-ethanol mixture and no PTM, respectively. The hydrostatic and nonhydrostatic experiments were pressurized to at least 12 GPa to ensure a full transformation to ω phase. The dynamic compression which enables a ramp compression and decompression in a temporal range of 0.001–1 s was controlled by piezoelectric actuator and arbitrary function generator. The parameters of dynamic load could be precisely modulated by the waveform of input signals to piezoelectric actuators. Pressure calibration was determined according to the redshift of R1 line of ruby and the equation of state of Pt foil. The dynamic parameters of comparative experiments were set into a ramp time of 0.001 and 1 s, which means the time a ramp compression run from pre-pressing (~1 GPa) to ~12 GPa. SXRD measurements were carried out at the 4W2 beamline of Beijing Synchrotron Radiation Facility (BSRF) for non-hydrostatic experiments and the beamline 15 U of Shanghai Synchrotron Radiation Facility (SSRF) for dynamic experiments. The wavelength of X-ray of BSRF and SSRF is 0.6199 and 0.6889 Å, respectively. Considering the pressure gradient caused in axial symmetry of DAC, diffraction data near the center of culet parallel to the direction of loading axis was collected. A MAR165 CCD detector is used for data collection, and the two-dimensional images is processed by the software DIOPTAS and subsequent analyzed through Rietveld refinement was used for lattice parameters and phase fraction of α- and ω-Ti. To decouple instrumental broadening, the data of standard sample CeO_2 was also measured. All reflections for TiB crystal were undetectable due to low mass fraction less than 5 %, thus the coupling effect of Ti and TiB is negligible in analysis.

2.3. Diffraction peak profile analysis

The conventional Williamson-Hall (cWH) method was initially used to determine the peak broadening of X-ray or neutron diffraction data based on the scattering vector of K ($= 2sin\theta/\lambda$). Thus the diffraction vector for the full width at half maximum (FWHM) can be expressed as ΔK ($= FWHM{\cdot}cos\theta/\lambda$), which reflects the overall contribution of instrument (ΔK_i), grain size (ΔK_D) and lattice distortion (ΔK_ε) on peak broadening. For most metals with anisotropic elastic properties, the modified W-H (mWH) method was further proposed by Ungár et al. by introducing a parameter, average dislocation contrast factor ($\overline{C}$), for specific planes [33,38]:

$$\Delta K = \left(\frac{0.9}{D}\right) + \left(\frac{\pi M^2 b^2}{2}\right)^{\frac{1}{2}} \rho^{\frac{1}{2}} K \overline{C}^{\frac{1}{2}} + \mathscr{O}\left(K^2\overline{C}\right) \tag{1}$$

The first and second term refers to the respective broadening from coherent domain (crystallite) size (D) and lattice-distortion-dependent variation in dislocation density (ρ) within the material [33,39]. In the second term, the M is a parameter of Wilken function and is related to the ρ and outer cut-off radius of dislocations R_e, and b is the modulus of Burgers vector. The average dislocation contrast factor for HCP crystal is derived as a generalized form of $\overline{C_{hk.l}} = \overline{C_{hk.0}}(1 + q_1x + q_2x^2)$,$x = (2/3)(l/Ka)^2$and the numerically calculated value of $\overline{C_{hk.0}}$, q_1, q_2 for all of eleven sub-slip-systems of HCP metals are available in elsewhere [32]. The experimentally measured values of $q_1^{(m)}$, $q_2^{(m)}$, which enable to determine the fraction of activated major slip systems with the Burgers vector type <a>, <c>, and <c+a>, can be drawn from the quadratic fit of the following equation:

$$\left[(\Delta K)^2 - \alpha^2\right]/K^2 = \beta\overline{C_{hk.0}}\left(1 + q_1x + q_2x^2\right) \tag{2}$$

where α, β stands for the quadratic form of the first and second term in Eq.1 when the $\overline{C}$ is substituted by $\overline{C_{hk.l}} = \overline{C_{hk.0}}(1 + q_1x + q_2x^2)$. The possible fraction of three major slip systems of HCP crystals, h_a, h_c, and h_{c+a}, can be calculated by ergodic combination of activated systems (N_A) in all eleven sub-slip-systems. Prior to the calculation the weighted averages of the theoretical $q_1^{(eff)}$, $q_2^{(eff)}$, are necessary to be introduced [40,41]:

$$q_{1,2}^{(eff)} = \frac{h_a b_a^2 \sum_{j=1}^{N_A^a} \overline{C_{hk.0}^{(J)}} q_{1,2}^{(j)} + h_c b_c^2 \sum_{j=1}^{N_A^C} \overline{C_{hk.0}^{(J)}} q_{1,2}^{(j)} + h_{c+a} b_{c+a}^2 \sum_{j=1}^{N_A^{c+a}} \overline{C_{hk.0}^{(J)}} q_{1,2}^{(j)}}{h_a b_a^2 \sum_{j=1}^{N_A^a} \overline{C_{hk.0}^{(J)}} + h_c b_c^2 \sum_{j=1}^{N_A^C} \overline{C_{hk.0}^{(J)}} + h_{c+a} b_{c+a}^2 \sum_{j=1}^{N_A^{c+a}} \overline{C_{hk.0}^{(J)}}} \tag{3}$$

The combination of h_a, h_c, and h_{c+a}, determined by Eq.3 is only considered valid if the $q_{1,2}^{(eff)}$ satisfies

$$q_{1,2}^{(m)} - \Delta q < q_{1,2}^{(eff)} < q_{1,2}^{(m)} + \Delta q \tag{4}$$

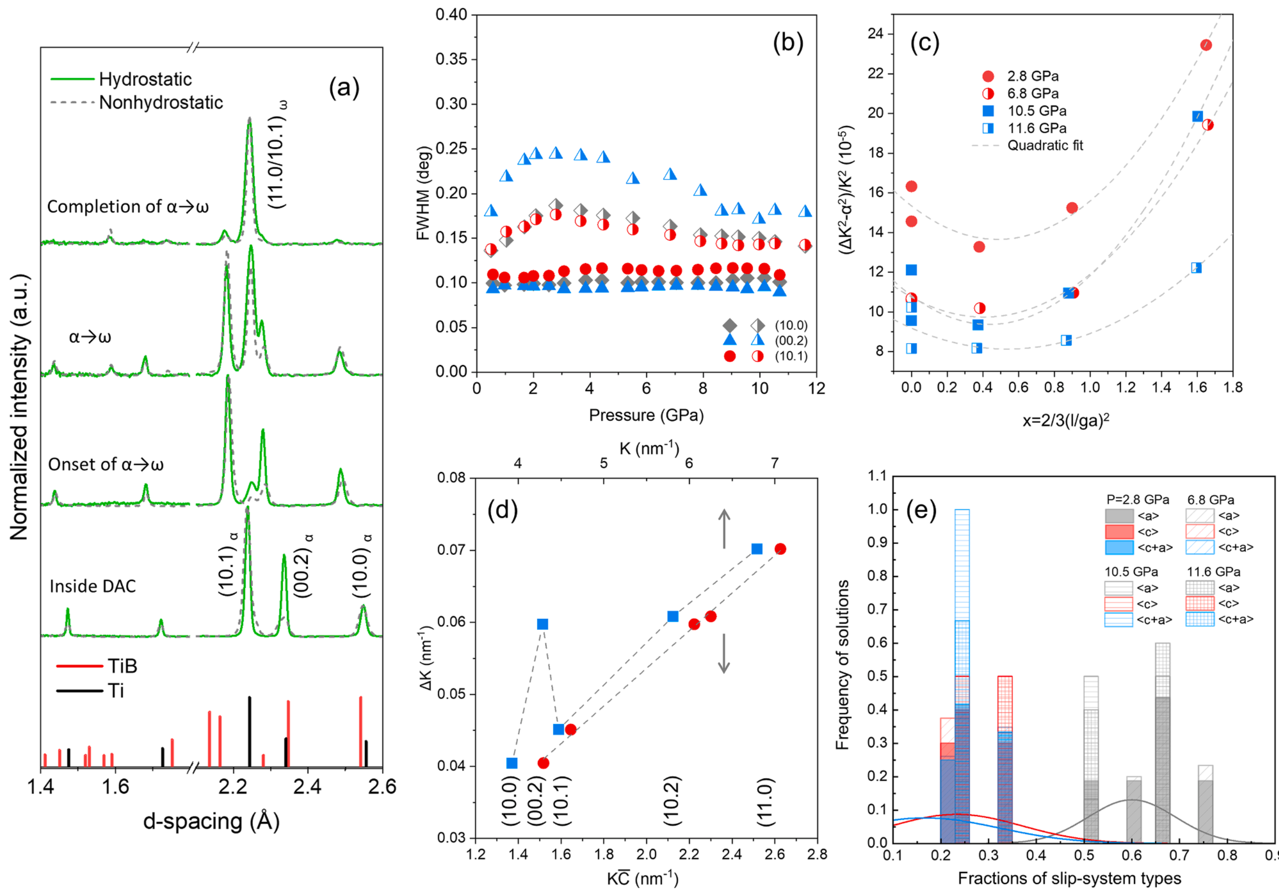

Fig. 2. Panoramic DPPA on dislocation evolution of Ti-TiB during plastic flow and strain-induced PT. (a) Representative SXRD profiles. (b) Pressure dependence of FWHM for main reflections of Ti-TiB at hydrostatic (solid) and nonhydrostatic (half-filled) pressures. (c) Determination of q parameters based on the mWH equation. (d) An example of strain anisotropy and its rescaling for all reflections of Ti-TiB at nonhydrostatic pressure of 6.8 GPa. (e) The histogram of the solution matrix of fractions of three Burgers vector types, <a>, <c> and <c+a>, activated in Ti-TiB at different pressures.

where the absolute tolerance Δq is 0.3 for HCP crystal according to the report by Ungár et al. [41]. Using the average value of h_a, h_c, and h_{c+a}, $\overline{b^2C_{hk.0}}^{(m)}$ can be written as

$$\overline{b^2C_{hk.0}}^{(m)} = \sum_{i=1}^{3} h_i \overline{C_{hk.0}}^{(i)} b_i^2 \tag{5}$$

The evaluation of the dislocation density is analyzed by the modified Warren-Averbach (mWA) method based on the Fourier transformation of reflections for HCP crystals as:

$$lnA(L) = lnA^S(L) - \rho\frac{\pi}{2}L^2\ln\left(\frac{R_e}{L}\right)\left(K^2\overline{b^2C}\right) + \mathscr{O}\left(K^2\overline{b^2C}\right)^2 \tag{6}$$

where L is the Fourier length and L=na$_3$ that is dependent on the measured diffraction profiles. The dislocation density ρ and the outer cut-off radius of dislocations R_e can be determined from the slope and intercept of linear regression between $Y(L)/L^2$ vs ln$L$, respectively:

$$\frac{Y(L)}{L^2} = \rho\frac{\pi}{2}lnR_e - \rho\frac{\pi}{2}lnL \tag{7}$$

where $Y(L) = -(\rho\pi L^2/2)\ln(R_e/L)$.

3. Results

3.1. Anomaly in α→ω PT of Ti-TiB under nonhydrostatic pressure

A general trend of remarkable reduction in critical pressure (P_c) of α→ω PT of CP-Ti has been observed when the hydrostaticity deteriorates [4,13,17,18,42]. For the worst condition of hydrostaticity (no PTM), the P_c usually scatters in a range of 3–9 GPa, and the completion occurs at ~12 GPa. As shown in Fig. 1b, the P_c value of Ti-TiB sample compares to the published data of CP-Ti in four common pressure environments, argon, 4:1 methanol-ethanol mixture, NaCl and no PTM. It is counter-intuitive to observe an unexpected increase in P_c of Ti-TiB when the deviatoric stress increases. In contrast to free constraint by GBs, this anomaly implies different responses and kinetic mechanisms of PT for α-Ti confined by stiff TiB boundaries to nonhydrostatic pressure. Relative phase fraction of α and ω in Ti-TiB and CP-Ti at hydrostatic and nonhydrostatic pressures exhibits *mechanically slow* and *fast* martensitic transformation for α-Ti confined by GBs and TiB networks, respectively [4] (Fig. 1c). Higher P_c and a narrow transition range of Ti-TiB were observed relative to CP-Ti regardless of hydrostaticity. In particular, upon nonhydrostatic pressure, the P_c of Ti-TiB is enhanced by ~5 GPa relative to CP-Ti, even slightly higher than Ti-TiB at hydrostatic condition [4]. Considering the difference between pressure-induced and strain-induced PT, knowing the dislocation evolution of Ti-TiB during plastic deformation and PT is crucial to reveal the role of TiB constraint in the corresponding pathway and kinetic of confined α-Ti at nonhydrostatic pressure.

3.2. Dislocation density evolution and activated slip systems

The strain broadening in XRD profile comes from the following aspects: (i) various defects, e.g., dislocations, twins and stacking faults, (ii) grain/sub-grain/phase boundaries, (iii) second-phase inclusions and

Table 1
The activated slip systems in α-Ti of Ti-TiB at nonhydrostatic pressures.

P (GPa)	$q_1^{(m)}$	$q_2^{(m)}$	$[h_{min},\ h_{max}]$			$\overline{h_a}$	$\overline{h_c}$	$\overline{h_{c+a}}$
			<a>	<c>	<c+a>			
2.8	-0.456	0.472	0.51–0.75	0.21–0.33	0.21–0.33	0.64	0.16	0.20
6.8	-0.461	0.568	0.51–0.67	0.25–0.33	0.25–0.33	0.60	0.23	0.17
10.5	-0.545	0.633	0.51–0.67	0.25–0.33	0.25	0.58	0.29	0.13
11.6	-0.427	0.398	0.51–0.75	0.21–0.33	0.21–0.33	0.65	0.14	0.21

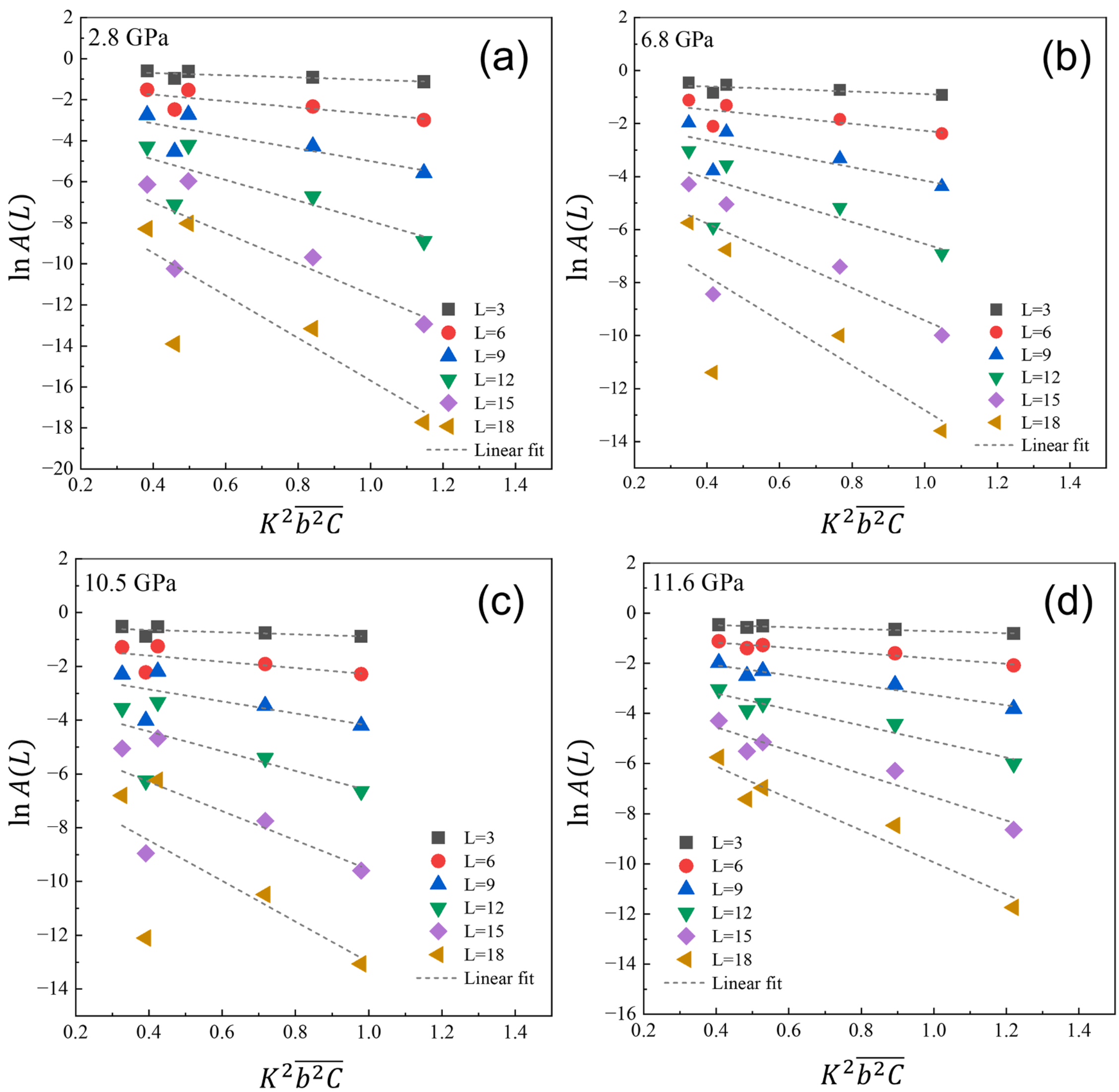

Fig. 3. The modified Warren-Averbach plots of Ti-TiB sample at stages of (a, b) severe plastic flow and (c, d) strain-induced α→ω PT.

precipitates, (iv) long/short-range internal stresses, (v) compositional inhomogeneity, etc. [43] Among them, dislocations and their interaction with other factors dominate the peak broadening of metals. In Fig. 2a, selected SXRD patterns of Ti-TiB during α→ω transformation are displayed. Due to small mass fraction, the Bragg reflections of TiB were not detected, while five reflections, (10.0), (00.2), (10.1), (10.2), (11.0), could be observed for α-Ti. Upon hydrostatic pressure, no obvious changes of microstrain and crystallite size in Ti-TiB can be concluded due to a negligible change of FWHM of three main reflections (Fig. 2b). In contrast, at nonhydrostatic pressure, remarkable broadening was found with a trend of first increasing to ~2.5 GPa, then decreasing till the occurrence of α→ω PT. The peak broadening of Ti-TiB at nonhydrostatic pressure is no doubt a combined outcome of increased microstrain and decreased crystallite size. In our previous report, Ti-TiB particles began to yield upon uniaxial stress at ~1.9–2.4 GPa by Tresca criterion [44]. This result may imply the transition of peak broadening as an indication of local yielding to global plastic deformation. In addition, the subsequent narrowing of FWHM of Ti-TiB may derive from the progressive relaxation of local stress commonly seen in nonhydrostatic experiments [45].

When the nonhydrostatic pressure was applied, the strain anisotropy in material was largely enhanced as shown in the conventional Williamson-Hall (cWH) plots for Ti-TiB samples at selected pressures of 2.8, 6.8, 10.5, and 11.6 GPa (Fig. S2). The former and latter two pressures correspond to the stages of severe plastic deformation and strain-induced PT, respectively. In Fig. 2c, the experimentally measured values

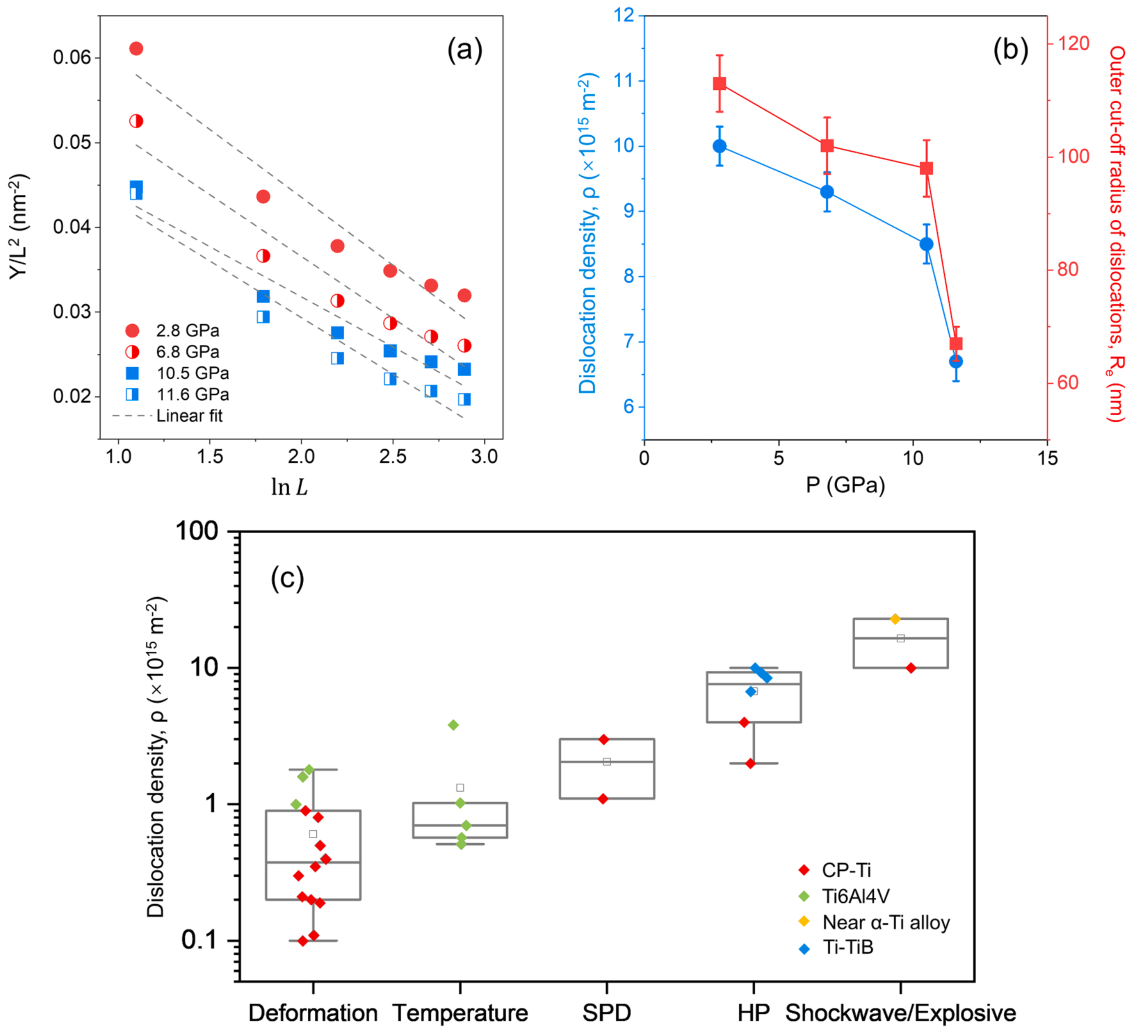

Fig. 4. The evolution of dislocation density of Ti-TiB upon nonhydrostatic pressure. (a) The linear regression of Y/L^2 as a function lnL based on Eq.7. (b) Dislocation density and effective outer cut-off radius of Ti-TiB as a function of pressure. (c) Comparison of mechanical/thermal-history-dependent dislocation density determined by DPPA for this work and literatures [32,36,46–50,54,55,59].

of $q_1^{(m)}$, $q_2^{(m)}$ can be determined by the quadratic curves from the relationship of $[(\Delta K)^2\text{-}\alpha^2]/K^2$ versus $x=2/3(l/ga)^2$. The average crystallite size D in Eq.1 deceases from 1.8 to 0.1 μm according to cWH method as the pressure increases. Though the crystallite size D is usually smaller than the real grain size due to the coherent size effect, the change in size still indicates the remarkable grain refinement in Ti-TiB samples at nonhydrostatic pressure. By introducing the value of $\overline{C_{hk.l}}$, the strain anisotropy of Ti-TiB samples at nonhydrostatic pressures can be rescaled linearly as manifested by an example at 6.8 GPa (Fig. 2d).

Then the histograms of relative fraction of three Burgers vectors, <a>, <c> and <c+a> for Ti-TiB samples at selected pressures are illustrated in Fig. 2e. We found that the valid slip combination of h_a, h_c, and h_{c+a}, for four sets of $q_{1,2}^{(eff)}$ is relatively rare compared to all possible combinations. As pressure increases, the fraction of activated slip systems for Ti-TiB samples varies within a narrow range as summarized in Table 1. It is found that a large fraction of <a> dislocations are activated while less than 30 % for other systems. In addition, the c/a ratio of Ti-TiB sample has no evident change as the pressure increases as shown in Fig. S3, also supporting the dominance of <a> slips in whole plastic deformation and PT. According to the average fraction of $\overline{h_i}$, the key parameter for the determination of dislocation density, $\overline{b^2C_{hk.0}}^{(m)}$, is calculated as 0.0247, 0.0227, 0.0207 and 0.0253 nm^2 by Eq.5 for above pressure conditions. These results agree well with 0.0222 nm^2 for plastically deformed Ti with a $\overline{h_i}$ combination of 0.75, 0.2, 0.05 from Ungár et al. [32], as well as 0.0249 nm^2 for Ti alloy with 0.89, 0, 0.11 from Muiruri, et al. [46]

Fig. 3 illustrates the mWA plots for Ti-TiB samples at four selected pressures by linking $lnA(L)$ versus $K^2\overline{b^2C}$ based on a set of values of Fourier length L (Eq.6). For the sample prior to transformation, the gradient of the data with higher values of L are seen to increase exponentially and displays increased divergence. In contrast, the data convergency becomes better for the sample compressed at 11.6 GPa. The scatter for higher L values indicates the assumption of small diffraction vector and Fourier length inherent in mWA method become less applicable for higher values.

According to the mWA method, the dislocation density and cutoff diameter of dislocations can thus be calculated by the linear regression of Eq.7 as shown in Fig. 4a. The value of R^2 for all fitting cases is larger than 0.94, indicating high goodness-of-fit. The dislocation density determined by the mWA method for Ti-TiB samples at four pressures achieve a high level of 10, 9.3, 8.5 and 6.7×10^{15} m^{-2} (Fig. 4b). The range of effective outer cut-off radius of dislocations fall within a range of 65–115 nm. For pristine Ti-TiB sample, the GND density is determined to be about 4.1×10^{14} m^{-2} by EBSD measurement (Fig. S4). This implies that a plethora of dislocations increased by at least one order of magnitude are activated during plastic deformation. The estimated dislocation density of Ti-TiB is further validated based on a wide range

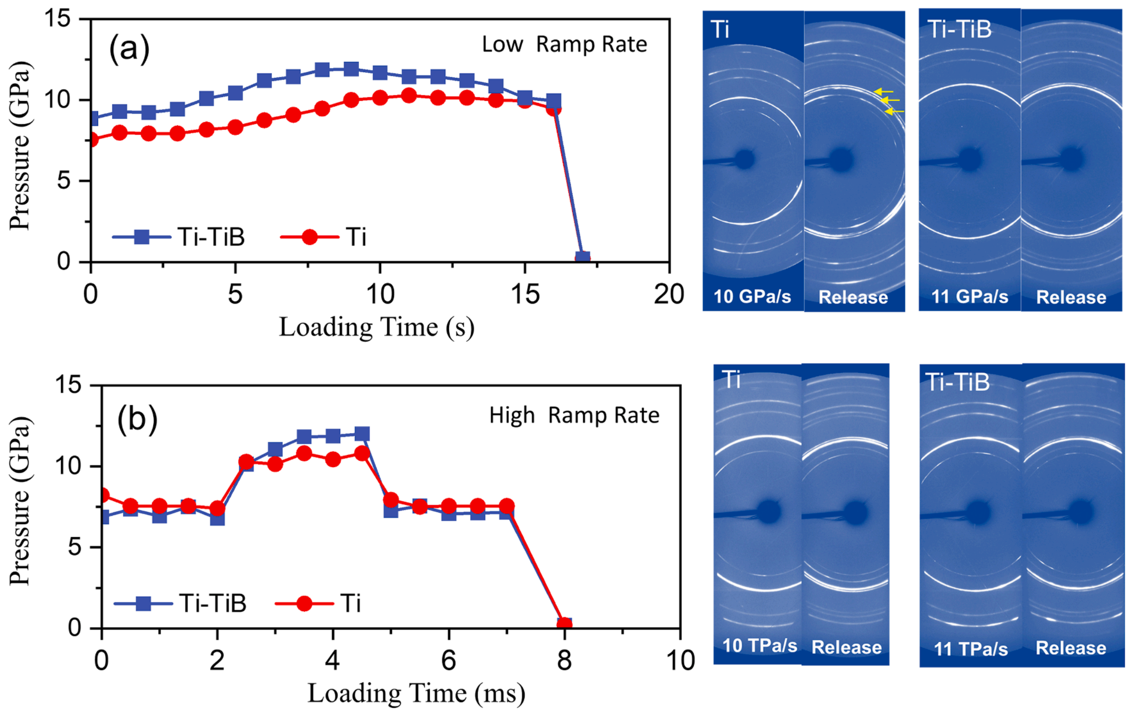

Fig. 5. Representative compression-decompression pathway in ramp compression and the Debye-Scherrer rings of high-pressure and recovered phases in CP-Ti and Ti-TiB samples at (a) low (~10–11 GPa/s) and (b) high ramp rates (~10–11 TPa/s). The main reflections of recovered α-Ti are indicted by the arrows.

of titanium samples upon different mechanical and/or thermal histories (Fig. 4c). For CP-Ti, a number of experiments showed that the dislocation density scatters in a range of 0.1–1×10^{15} m^{-2}, depending on the degree of deformation [47–49]. When CP-Ti undergoes severe plastic deformation, a large population of dislocations will be activated to 1–3×10^{15} m^{-2} [32,50,51]. At high pressure, the nonhydrostatic compression usually leads to the onset of martensitic transformation of CP-Ti less than 5 GPa under the condition of no PTM. Based on the report by Errandonea et al., we estimated the dislocation density of CP-Ti compressed in NaCl in a range of 2–4 ×10^{15} m^{-2}, and see details of the mWH analysis in Fig. S5. This estimation is close to a recent report on dislocation density (~1.26–1.83 ×10^{15} m^{-2}) in α-Zr at the initiation of α→ω PT [52]. If the hydrostatic loading was applied, then the dislocation densities in annealed and pre-deformed Zr decreased, and scattered in the level of 10^{14}–10^{15} m^{-2} [53]. Complex scenario of dislocation evolution was observed in Ti alloys due to the coexistence of dual phases and various alloying elements. Taking Ti6Al4V as an example, uniaxial tension led to 0.9–1.8 ×10^{15} m^{-2} as the strain increased from 1–8 % [54,55], while the rapid solidification process of additive manufacturing caused high density of 3.8×10^{15} m^{-2} [46]. Post-annealing significantly reduced the dislocation density of as-built Ti6Al4V to a low level of 5.1×10^{14} m^{-2}. Extreme loading is no doubt to trigger more deformation mechanisms that is hard to activate under common conditions. Upon shockwave loading, the dislocation density of CP-Ti can achieve as high as 1×10^{16} m^{-2} with less activated twins, indicating the major contribution of slip on dislocation density enhancement at high pressure and high strain rate [56]. Even higher dislocation density of 2.3×10^{16} m^{-2} was reported in a near-α Ti alloy under explosive loading [57]. Although the nature of Ti and TiB is compatible and their interfaces are coherent/semi-coherent, interfacial misfit and strain gradient is inevitably introduced and micro-distortions around second-phase inclusions will be generated during fabrication and deformation [58]. Section 4.3 will discuss the stress gradient and dislocation evolution associated with heterogeneous effect of Ti-TiB during deformation and transformation.

In addition, since α- and ω-Ti have different lattice constants, their dislocation behaviors during PT should be different. In this work, however, we focused on the dislocation analysis on dominant α-Ti due to the following reason. The dislocation multiplication in newly formed ω-Ti might be not as significant as that subjected to subsequent deformation. As shown in Fig. S6, the width of main diffraction peak of newly formed ω-Ti is as narrow as initial α-phase, probably indicating a low dislocation density and less activated systems. Upon further pressurization, the obvious broadening of diffraction peak of ω-Ti displayed enhanced microstrain and dislocation density.

3.3. Anomaly in ω→α transformation of Ti-TiB under dynamic nonhydrostatic pressure

Dynamic pressure (ramp compression) experiments performed by dDAC enable the investigation of kinetics and metastable phase of materials up to several tens of gigapascal in a time-resolved level of millisecond [60]. The α→ω PT of CP-Ti at dynamic pressure was found to be delayed to an intermediated critical pressure between static and shock compression experiments, indicating the compression-rate-dependence of PT kinetics [61,62]. At high ramp rate of 73 GPa/s, the transition onset is delayed to 12.5 GPa and enhanced stability of α-Ti was observed [61]. Huston et al. further reported that the differential stress and texture of CP-Ti also depends on pressure and ramp rate by utilizing radial dDAC [63]. Note that all above experiments were performed in a single ramp compression-decompression run. In order to explore the influence of TiB constraint on the structural stability and the recovery hysteresis of ω-Ti, comparative experiments of cyclic ramp compression (N~10,000) were conducted using CP-Ti and Ti-TiB samples at low ($\frac{dP}{dt}$ ~10 GPa/s) and high ramp rates (~10^4 GPa/s). The compression-decompression pathway at the last run and the corresponding Debye-Scherrer rings of high-pressure (ω) and recovered (α+ω) phases in CP-Ti and Ti-TiB are plotted in Fig. 5. For clarity, the mask grid is not shown but the pixels in a mask is screened off in data analysis. As shown in the loading pathway, the CP-Ti and Ti-TiB samples were repeatedly compressed in a range of 7.5–11 GPa and 8–12 GPa, respectively. This operation makes sure a full completion of ω-phase in both groups. As shown in diffraction rings, only ω-Ti at low ramp rate

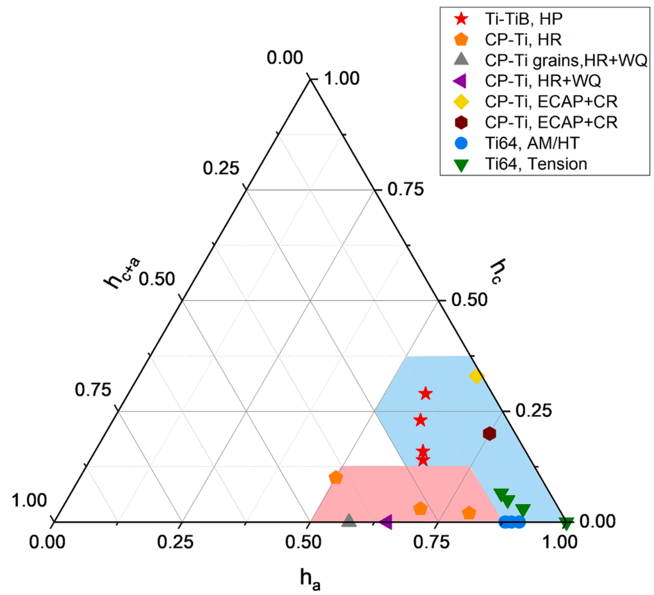

Fig. 6. The average Burgers vector fraction, $\overline{h_a}$, $\overline{h_c}$, and $\overline{h_{c+a}}$, activated in Ti-TiB, CP-Ti and Ti alloys upon different mechanical and thermal histories. The activation preference of <c> and <c+a> slip systems to deformation or temperature is illustrated by blue and red regions, respectively. (For interpretation of the references to colour in this figure legend, the reader is referred to the web version of this article).

could largely recover, and main reflections of (10.0), (00.2), (10.1) of α-Ti reemerged as marked by the arrows. High ramp rate and TiB constraint were found to be kinematic barriers for ω→α PT. Possible reasons will be discussed in Section 4.5.

4. Discussion

4.1. Yield strength of Ti-TiB at high pressure

The change of yield strength associated with high pressure PT is essential to understand the mechanism underlying the PT-driven plasticity [21,64]. For metals under pressure, yield strength (σ_y) usually equals the macroscopic differential stress (t=σ_{33}-σ_{11}=σ_y) and the flow stress will be saturated with the increase of strain hardening [65]. The macroscopic differential stress $t = \sigma_{ij} - P$ is derived from the Hooke's law ($\sigma = E\varepsilon$) and its maximum value is the derived yield strength for a given pressure. If we take the onset of global plasticity as yield point, then the macroscopic differential strain (ε) of α-Ti-TiB composite at ~2 GPa by averaging lattice strain equals 0.006±0.001 (Fig. S7). The derived σ_y achieves approximately 732±122 MPa, when the elastic modulus E is calculated by $E = 3K(1 - 2\nu)$, where K is the isothermal bulk modulus (~120 GPa) derived from EOS of Fig. S8 and ν the Poisson's ratio (~0.33). The derived σ_y of α-Ti-TiB composite is close to the value of ~751±100 MPa determined by the mixing rule for composites by taking the set of strength of CP-Ti ~496±100 MPa [44] and TiB ~8000 MPa [66]. Due to the particle geometry, the Ti-TiB sample will undergo elastic, local yielding and global plastic deformation when subjected to nonhydrostatic compression. Simultaneously, densification and strain hardening also increases continuously at nonhydrostatic pressure. Again, according to the mixing rule, the yield strength of ω-Ti-TiB composite is approximately assessed to be ~1154 MPa based on the reported compressive strength of ~913 MPa for bulk ω-Ti [59]. Thus, the ratio of yield strength of ω/α of Ti-TiB is ~1.5, lower than that of Ti (~1.8) and Zr (~2.1) [21,59], showing the pronounced reinforcing effect of TiB network on the yielding of α-Ti.

4.2. Influence of TiB constraint on the activation of slip systems

In Fig. 6, the combination of average Burgers vector fractions for deformed CP-Ti and other titanium alloys are mainly scattered near the corner of $\overline{h_a}$-$\overline{h_c}$ axis, indicating the massive activation of prismatic <a> and basal <a> dislocations [32,36,46,48,49,54,55]. Note that the common twinning systems, i.e., $\{10.1\}\langle 10.\overline{2}\rangle$ and $\{11.2\}\langle 11.\overline{3}\rangle$ compressive twins and $\{10.2\}\langle 10.\overline{1}\rangle$ and $\{11.1\}\langle \overline{11}.6\rangle$ tensile twins, are not discussed herein due to small fraction of twins are activated during deformation [48]. Even the deformation twins could saturate in HCP crystal at a certain condition, the twin density is still far lower than dislocation density [67]. An interesting fact was found that the activation of <c> and <c+a> in CP-Ti and alloys seems sensitive to deformation and temperature, respectively. Similar activation preference of the fraction, range of h_a, h_c, and h_{c+a} to the deformation/temperature history was also observed in other HCP crystals, such as Mg [40] and Zr [41]. Considering the preparation process and structural heterogeneity of a composite, the difference in thermal expansion coefficient between second-phase inclusions and matrix will cause micro-distortions around those inclusions [68]. When Ti-TiB undergoes plastic deformation, a plethora of dislocations are generated and pile-up near Ti/TiB interfaces, further increasing the local stress concentration and strain gradient near interfaces. Deviatoric stress can also stimulate additional slip systems that are hard to activate at ambient conditions. These reasons probably account for the relatively high population of <c> and <c+a> dislocations during plastic flow and strain-induced PT of Ti-TiB.

4.3. Long-range internal stress and the evolution of GND

Among various microstrain-induced defects, deformation-induced long-range internal stress and lattice misorientations also evolves as important features of heterogeneous dislocation distribution during the deformation of crystalline materials. In order to determine long-range internal stress and the corresponding GNDs in the plastic strain of heterogeneous regions, the Mughrabi's composite model for multiple slips was proposed [69]. Here, simple modification was made to accommodate to a Ti-TiB cell according to the structural similarity. As shown in Fig. 7a-7b, if the local shearing the Ti cells and TiB walls endured are τ_{Ti} and τ_{TiB}, respectively, the macroscopic differential stress τ and the corresponding deformation-induced long-range internal stresses, that is, the back stress $\Delta\tau_{Ti}$ and the forward stress $\Delta\tau_{TiB}$, can be linked as follows:

$$\tau_{Ti} = \tau + \Delta\tau_{Ti} = \tau - G_{TiB}\Gamma f_{TiB}\Delta\gamma_p \quad (8)$$

$$\tau_{TiB} = \tau + \Delta\tau_{TiB} = \tau + G_{Ti}\Gamma f_{Ti}\Delta\gamma_p \quad (9)$$

where G is the shear modulus of respective phases, Γ is Eshelby's elastic accommodation factor (Γ≤1), f_{Ti} and f_{TiB} are the volume fraction of Ti and TiB. Assuming the TiB walls hardly deform during plastic deformation and PT, $\Delta\gamma_p$, the mismatch of plastic strain near Ti/TiB interface can be defined as:

$$\Delta\gamma_p = \Delta\varepsilon_V \big/ (1 - 2\nu) \quad (10)$$

$$\varepsilon_V = \varepsilon_{xx} + \varepsilon_{yy} + \varepsilon_{zz} \quad (11)$$

$$\varepsilon_{xx} = \varepsilon_{yy} = -\nu\varepsilon_{zz} \quad (12)$$

where the $\Delta\varepsilon_V$ is the difference of volumetric strain between Ti-TiB and CP-Ti at identical pressure conditions including the magnitude and environment of pressing, and ε_{xx}, ε_{yy}, is the radial linear strain and ε_{zz} the axial linear strain, ν the Poisson's ratio. For simplicity, ideally symmetric multiple slips and no lattice misorientations will be expected. Axially internal stress activates the pairs of dislocation with Burgers vectors b_1 and b_2 on two symmetric slip systems. These dislocation pairs

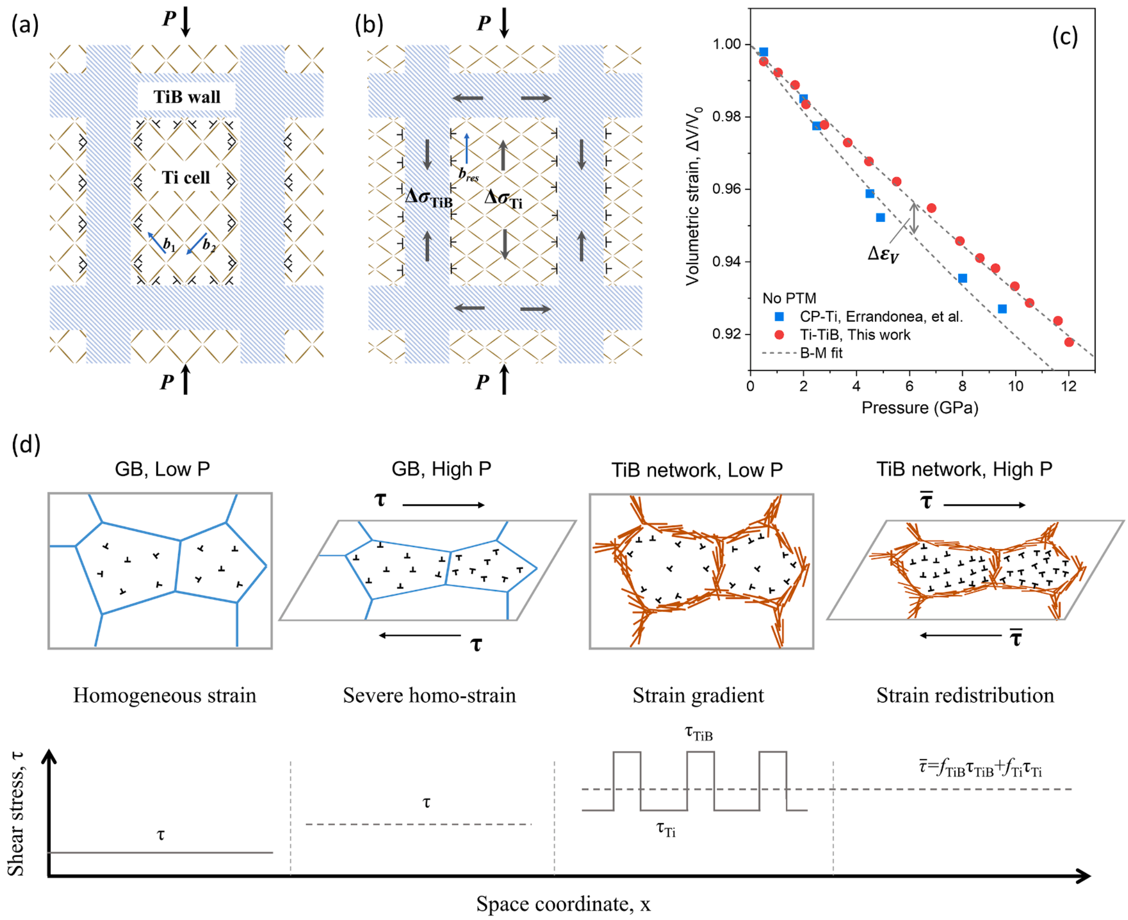

Fig. 7. Modified Mughrabi's composite model for a Ti-TiB cell under uniaxial stress. (a) Schematic of multiple slips with the generation of GNDs. (b) Long-range internal stress of the composite under uniaxial compression and the equivalent replacement of Burgers vectors b_1, b_2 to b_{res}. (c) The volumetric strain and the corresponding fit of Birch–Murnaghan EOS of CP-Ti and Ti-TiB as a function of pressure. (d) Schematic illustration of shear strain mismatch and flow stress distribution in Ti grains with GBs and TiB network at low and high nonhydrostatic pressures.

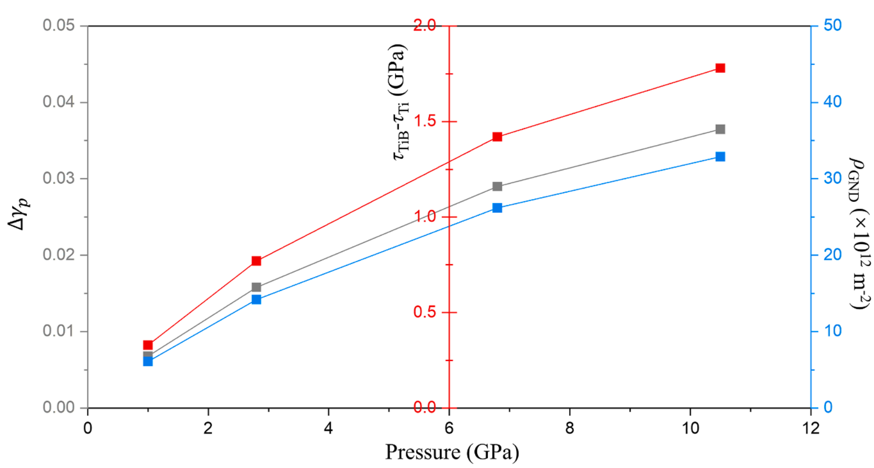

Fig. 8. Evolution of long-range internal stress, GND density, strain mismatch of a Ti-TiB cell at nonhydrostatic pressure. The values of axial linear strain, ε_{zz}, the stress difference of Ti/TiB interface, τ_{TiB}-τ_{Ti}, and GND density near Ti/TiB interface as a function of nonhydrostatic pressure.

can be further considered as resultant dislocations with b_{res} lying parallel to the stress axis as illustrated in Fig. 7b See obvious difference of volumetric strain between Ti-TiB and CP-Ti upon nonhydrostatic compression in Fig. 7c. To illustrate the difference of long-range internal stress and the corresponding GND evolution in CP-Ti and Ti-TiB, the model of strain gradient of Ti-TiB sample at high pressure is established (Fig. 7d).

According to above model, by averaging the density of the GNDs over the cell spacing d, the mean GND density can be calculated by:

$$\rho_{GND} = 2(\tau_{TiB} - \tau_{Ti})/b_{res}Ed \quad (13)$$

Thus, the evolution of axial linear strain, ε_{zz}, the stress difference of Ti/TiB interface, τ_{TiB}-τ_{Ti}, and the GND density of Ti-TiB sample during plastic deformation and PT can be estimated using the set of values:

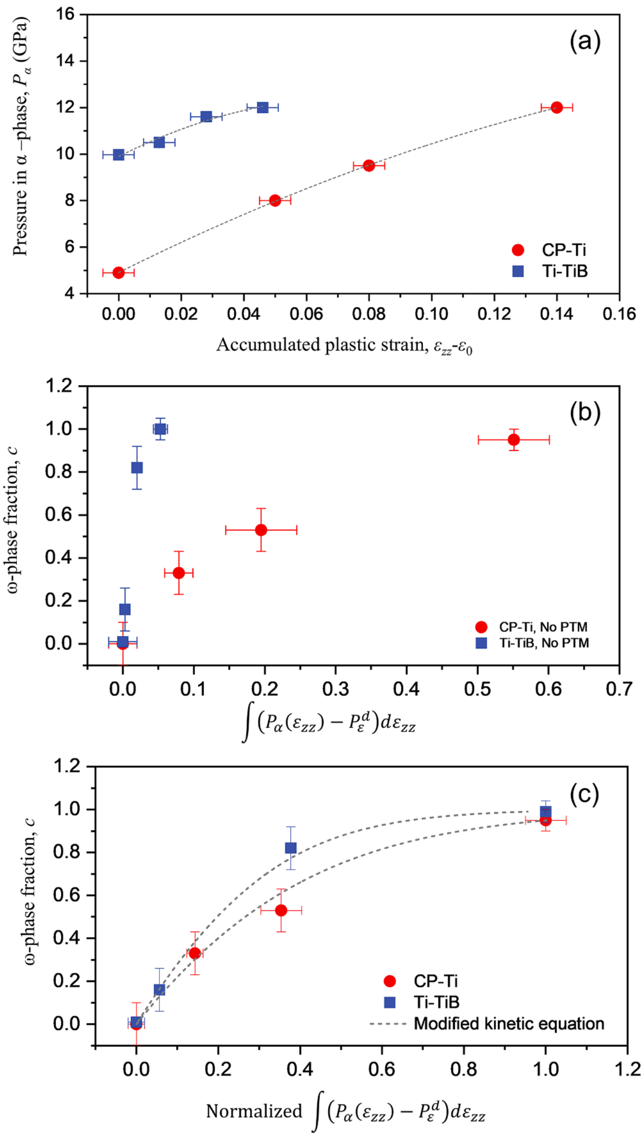

Fig. 9. Analytical kinetics of strain-induced PT of Ti-TiB and CP-Ti under nonhydrostatic pressure. (a) Pressure in α-phase, P_α, as a function of accumulated plastic strain, $\varepsilon_{zz}-\varepsilon_0$. Strain-induced kinetics of α→ω transformation in Ti-TiB and CP-Ti in (b) original form of Levitas's equation and (c) its normalization.

G_{TiB} = 185 GPa [70], G_{Ti} = 44 GPa, b_{res} =0.295 nm, $E_{Ti\text{-}TiB}$=122.4 GPa, d=3 μm, f_{TiB}=3.4 %. As shown in Fig. 8, the deformation-induced long-range internal stress and the corresponding GND density increases monotonically with the increase of axial linear strain. In particular, the ρ_{GND} regarding to interfacial strain gradient falls within a range of 6.1–32.9 $\times 10^{12}$ m^{-2} from 1 to 10.5 GPa. Compared to the DPPA results, heterogeneous deformation-induced GND density near Ti/TiB interfaces accounts for a small fraction of ~0.5 % relative to total dislocation density, close to the case of persistent slip bands consisting by dislocation walls in fatigued metals [71,72]. This may be explained by the limited proportion of heterogeneous regions consisting by TiB (boundary width~150 nm) relative to the grain size of α-Ti with an average size of ~3 μm. The heterogenous effect in plastic deformation is expected to be pronounced if the relative size of second-phase-rich regions increases and the proportion of coarsen/fine grains is appropriate [73]. However, it is worth noting that the local stress near Ti/TiB interfaces was in a gigapascal level and the maximum achieved as high as 1.78 GPa. The relief of such high local stress may boost the atomistic shuffling, thus the PT of α-Ti embraced by heterogeneous interfaces could complete in a narrow pressure range.

4.4. Kinetics of strain-induced PT in α-Ti of Ti-TiB

The theory of strain-induced kinetics for the PTs of materials at high pressure was proposed by Levitas et al. based on the nanoscale mechanism [22,74]. For normal PT with $P_\alpha > P_\varepsilon^d$, there exists a simplified formula [21,22]:

$$\frac{dc}{d\varepsilon} = \frac{k(1-c)\left(\sigma_y^\omega / \sigma_y^\alpha\right)^w}{c + (1-c)\left(\sigma_y^\omega / \sigma_y^\alpha\right)^w} \frac{P_\alpha - P_\varepsilon^d}{P_h^d - P_\varepsilon^d} \tag{14}$$

see the definition of parameters and theoretical assumptions in Refs [21, 22]. In order to ensure that this formula obeys the basic principle and is applicable to general DAC experiments, the original accumulated plastic strain determined by the variation of sample thickness can be reasonably replaced by the axial linear strain (ε_{zz}) along the loading axis of non-hydrostatic compression. Note that the influence of pressure gradient along the radial direction can be neglected if the data was collected near the center of culet. In order to describe the dependence of strain-induced transformation on loading path, the relationship of the pressure in the α-phase (P_α) against accumulated ε_{zz}, for Ti-TiB and CP-Ti under non-hydrostatic compression is plotted in Fig. 9a. It was found that the accumulated axial strain required to complete α→ω PT for CP-Ti is three times larger than that for Ti-TiB. This is also able to explain above result of dislocation density in Ti-TiB and CP-Ti differs by a factor of ~2–4. To establish the strain-induced kinetics, the integral form of Eq.14 is required:

$$c(B-1) - \ln(1-c) = \frac{kB}{P_h^d - P_\varepsilon^d} \int_0^{q-q_0} \left(P_\alpha(x) - P_\varepsilon^d\right) dx, \; B = \left(\frac{\sigma_y^\omega}{\sigma_y^\alpha}\right)^w \tag{15}$$

Then the kinetics of ω-Ti could be described by virtue of the strain-dependent integral term of Eq.15 as shown in Fig. 9b The CP-Ti and Ti-TiB completed α→ω PTs through different accumulated strains, and a large difference of $\int_0^{q-q_0} (P_\alpha(x) - P_\varepsilon^d) dx$ was found for Ti-TiB and CP-Ti of ~0.1 and ~0.6 GPa, respectively. In principle, however, the kinetic equation could not reflect the contribution of accumulated dislocation quantity on the nucleation of ω phase prior to the onset of α→ω PTs. Thus, the strain-controlled parameter $\int_0^{q-q_0} (P_\alpha(x) - P_\varepsilon^d) dx$ was further normalized and the divergency on different strain paths for the same PT can be eliminated (Fig. 9c).

4.5. Influence of TiB constraint on phase recovery

The brightest rings for CP-Ti and Ti-TiB in Fig. 5 represent the reflection of $(11.0/10.1)_\omega$ plane and the broadening of integral lines shows sensitivity to boundary configuration and ramp rate (Fig. 10a). At low ramp rate, the $(11.0/10.1)_\omega$ plane of CP-Ti was a bit more compressible relative to Ti-TiB as evidenced by a small shift of 0.01 Å to the direction of lattice compression. Similar broadening of FWHM denoted a limited microstrain. When the pressure was released, however, a large fraction of residual ω-Ti was observed in Ti-TiB, while an opposite scenario for CP-Ti (Fig. 10b). It demonstrates that the heterogenous constraint of TiB network also act as a kinematic barrier on the phase recovery during reverse PT. High-ramp-rate compression could lead to larger lattice distortion and the reflections of $(11.0/10.1)_\omega$ planes in both cases broaden significantly compared to low-ramp-rate experiments. Simultaneously, the $(11.0/10.1)_\omega$ plane of CP-Ti was highly compressed and showed a larger peak shift of 0.03 Å. For Ti-TiB, the

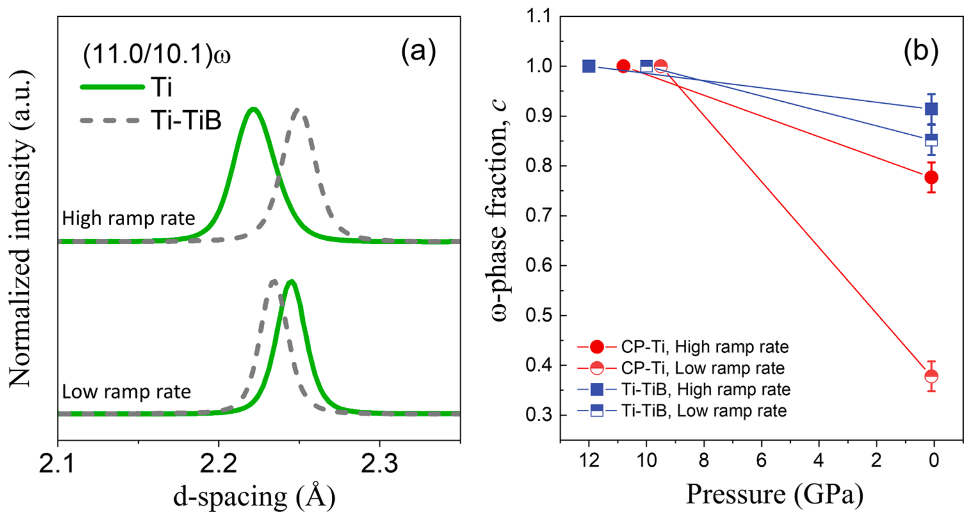

Fig. 10. Kinetic suppression in reverse PT of α-Ti in Ti-TiB under cyclic dynamic pressure. (a) Peak broadening of (11.0/10.1) reflections of ω-Ti in CP-Ti and Ti-TiB. (b) The retention of ω-phase in CP-Ti and Ti-TiB at indicated conditions.

heterogeneous constraint by TiB was demonstrated to provide effective resistance to dynamic lattice shearing and recovery whether at high or low ramp rate. Although the in-situ diffraction profile during decompression were unavailable, the mechanism can be understood by theoretical studies. Briefly, the recovery kinetics of reverse PT in Ti is also controlled by heterogeneous nucleation from microstructural defects. According to the atomistic simulation by Zong et al., defects can act as either heterogeneous nucleation centers or obstacles for the migration of the martensitic interfaces [75].According to the high dislocation density observed in forward PT, the difficulty in recovery of ω-phase in Ti-TiB is thus understandable because there exists a large population of activated defects to hinder the movement of α/ω interfaces to recover.

4.6. Revisiting the P-T diagram of Ti

Let's recall the classic pathways proposed by Silcock and Trinkle et al., the six-atom shuffling of α cell to final ω phase obeys simple ORs as follows: $(00.1)_\alpha \parallel (0\bar{1}1)_\omega$, $[11.0]_\alpha \parallel [01.1]_\omega$[12], or $(00.1)_\alpha \parallel (11.0)_\omega$, $[11.0]_\alpha \parallel [00.1]_\omega$ [14]. In terms of kinetics, lattice shearing could be easily satisfied by the enhancement of deviatoric stress tensors, thus the martensitic PT will be promoted due to the heterogenous nucleation of ω embryo from microstructural defects, e.g., dislocations and α/ω interfaces [19,75]. Molecular dynamics also revealed that moderate deviatoric stress either from applied load or internal stress of dislocations significantly promote the PT by reducing the critical radius of stable ω embryo. The interaction of activated prismatic dislocations with α/ω interfaces was found to favor the growth of ω embryo [19]. Or, to be more specific, prismatic <a> dislocations and {10.2} twins promote the PT more effectively than pyramidal <c+a> dislocations and {11.2} twins [23]. Oppositely, high compression rate and interstitial elements were found to suppress α→ω PTs and the reason is due to the microstructure changes, for example, twinning, slip planarity, and texture [15, 61,63].

The scenario of α→ω PT of Ti-TiB is complex due to heterogeneous stress/strain induced by TiB network and their interactions with dislocations. First, our result of SXRD supports that the PT of Ti-TiB also proceeds with the Silcock mechanism and no other intermediate phase was detected, indicating negligible effect of structural heterogeneity on the α→ω pathway. Second, the heterogeneous constraint of TiB strongly impact the kinetics of PT of Ti as mentioned above. At initial plastic stage, α-Ti grains first undergo deformation and then TiB network deforms coordinately. The total dislocation density will increase rapidly, accompanied with the activation of commonly inactive <c> and <c+a> slip systems. Heterogenous stress/strain at this stage is still far from reaching a level to influence the PT. Then, the plastic flow becomes saturated by a certain level of strain hardening from dislocation multiplication, and a plethora of dislocations start to move and pileup at Ti/TiB interfaces. Due to the flow is steady and a certain of local stress is relaxed, additional slip systems are no longer needed to maintain the flow deformation. As the nonhydrostatic pressure increases, the interfacial mismatch of Ti/TiB becomes remarkable and strong Zener pinning of TiB whiskers causes heterogeneous strain near interfaces and an increased fraction of nonhydrostatic pressure could be borne by TiB network. Although high dislocation density favors the nucleation of ω phase, the lattice shearing of local regions is alleviated by stress partition and the driving force for the growth of ω embryo is suppressed. When entering the stage of PT, the threshold of nonhydrostatic pressure to boost the growth of critical ω embryo in Ti-TiB is enhanced by ~5 GPa relative to that for CP-Ti. Other factors may also contribute to the suppression of PT, such as grain refinement and nanowhiskers with high aspect ratio. In particular, TiB nanowhiskers with high aspect ratio is superior to other reinforcements and significantly strengthen the matrix [76,77]. High aspect ratio of TiB not only refine the grains effectively but the Ti/TiB interfaces with high bonding strength transfer load and tangle with dislocations. It is also worth noting that Levitas and co-authors had conducted theoretical study on the kinetics of strain-induced PT for multiphase materials with homogeneous, non-transforming particles [78]. The homogeneous distribution gives rise to a small strain gradient near the interfaces of matrix and secondary phases, and the global plastic flow will readily achieve. This might be one of the reasons why stronger non-transforming particles increase plastic strain in the rest of material. However, the heterogeneous distribution of secondary phases can strongly change the stress/strain partition of flow plasticity either in deformation or PT. Thus, TiB nanowhiskers located at the GBs displayed a much stronger effect on the mechanism of plastic flow and PT than that of particles in Ref [78].

From a perspective of equilibrium PT of Ti, several factors are crucial on the control of phase stability and boundary of α→ω PT of Ti, including hydrostatic pressure [79], deviatoric stress [4,19], compression rate [61,63], grain size and interstitial elements [15,16]. In most literature, the triple point of α-ω-β reported by either Tonkov, et al. (8 GPa, 913 K [80]) or Zhang, et al.(7.5 GPa, 913 K [81]) is usually adopted. In principle, trace B element and TiB will not affect the α-β transition, therefore, it can be inferred that less influence on ω-β transition. Experimental constraint of α-ω boundary can be simply determined by the extrapolation of onset pressure (P_c) or median pressure for α/ω mixture ($P_{\alpha+\omega}/2$)

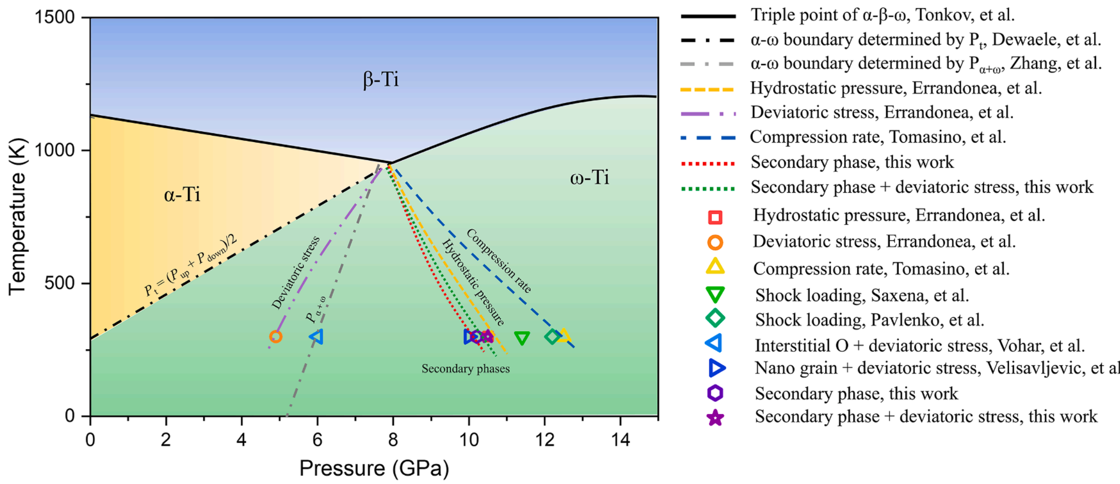

Fig. 11. Phase diagram of Ti and the tentative phase boundaries of α-ω phases, which depends on the factors such as hydrostatic pressure, deviatoric stress, compression rate, secondary phases [79–81]. Hollow symbols refer to the onset pressures of α→ω transformation of Ti at various conditions at room temperature [4, 13,56,61,82,83]. Note that the tentative phase boundaries were determined by the reported triple point and intermediate pressure for the coexistence of α and ω phases [81].

at room temperature to triple point [80,81]. The data of onset pressure of PT are well documented in most literature, enabling a direct comparison of tentative α→ω boundary by linking experimental data at room temperature with triple point. As shown in Fig. 11, we could see clearly the presence of TiB network could compensate most of shape variation induced by deviatoric stress and make α-Ti transform in a hydrostatic-like behavior under nonhydrostatic pressure. Heterogenous constraint could enhance the region of stability of α-Ti and provides kinetic barrier for both forward and reverse PT.

5. Conclusions

The first in-situ investigation of heterogeneous effect of secondary phases on the plastic deformation and strain-induced PT of α-Ti under nonhydrostatic and dynamic pressures has been scrutinized using DPPA and analytical models. Comparative studies between CP-Ti and Ti-TiB revealed the influence of strong heterogeneous constraint on the evolution of dislocation density, activated slip systems and phase fraction in α-Ti during severe plastic flow and strain-induced α→ω PT. Based on experimental and analytical results, the abnormal kinetic suppression in forward and reverse PT of Ti-TiB have been reasonably interpreted. Main conclusions are obtained as follows:

(i) The highest dislocation density in a magnitude of $\sim 10^{16}$ m^{-2} is found when the Ti-TiB enters a global plastic deformation at ~2.8 GPa. As the pressure increases, the dislocation density stabilizes in a range of 8–9×10^{15} m^{-2} during stable plastic flow. At the stage of strain-induced PT, the dislocation density further decreases and the value for the completion of PT is about 6.7×10^{15} m^{-2}. The variation of dislocation density denotes a competition between microstructural events such as dislocation multiplication and nonhydrostatic pressure relief.

(ii) Ergodic analysis yields the combination of <a>, <c> and <c+a> dislocations with an average fraction of 0.62, 0.2, 0.18 during the whole deformation and PT of confined α-Ti in Ti-TiB. Compared to severe plastically deformed CP-Ti, our results indicate more prismatic and pyramidal <c+a> dislocations are probably activated under heterogeneous constraint.

(iii) Long-range internal stress at Ti/TiB interface increases monotonically with the pressure, and the stress difference could achieve as high as 1.78 GPa, though the corresponding GND density takes a small fraction of total dislocation density. Although severe plastic deformation produces more heterogeneous sites for ω nucleus in confined α-Ti, the heterogeneous-stress-partition of TiB network probably suppress the α→ω PT.

(iv) The kinetics of strain-induced α→ω PT in Ti-TiB is predicted and agrees well with that for CP-Ti using the nanoscale mechanism-based equation if the accumulated axial linear strain is employed and the strain-controlled parameter $\int_0^{q-q_0} \left(P_\alpha(x) - P_\varepsilon^d\right)dx$ is normalized.

(v) Cyclic dynamic experiments show that over 85 % volume fraction of ω-Ti phase can be retained in Ti-TiB, regardless of ramp rate, showing the remarkable resistance of TiB network to the recovery of metastable phase. In contrast, the results for CP-Ti display a weak confinement of GBs against reverse PT and a ramp-rate-dependent recovery kinetics.

(vi) The tentative phase boundaries of α-ω phases of Ti affected by the heterogeneous effect of secondary phase has been established based on the extrapolation of critical pressure of Ti-TiB to theoretical triple point.

CRediT authorship contribution statement

Bo Li: Writing – original draft, Supervision, Investigation, Formal analysis, Conceptualization. **Chenhui Hu:** Investigation, Formal analysis. **Kaiyuan Shi:** Validation, Investigation, Formal analysis. **Lei Su:** Writing – review & editing, Validation, Supervision, Methodology, Funding acquisition. **Yizhe Cao:** Investigation. **Huiying Liu:** Investigation. **Dongxu Hui:** Investigation. **Shaodi Wang:** Investigation. **Chuanwei Fan:** Software, Formal analysis. **Katsuyoshi Kondoh:** Formal analysis. **Xin Zhang:** Formal analysis. **Shengyin Zhou:** Formal analysis. **Shufeng Li:** Supervision, Resources, Project administration, Funding acquisition.

Declaration of competing interest

The authors declare that they have no known competing financial interests or personal relationships that could have appeared to influence the work reported in this paper.

Acknowledgements

The authors acknowledge the financial support of National Natural Science Foundation of China (Grant No. 52471162), Key Research Plan

Project of the Shaanxi Provincial Department of Education - Key Laboratory Project (No. 24JS034), and Shaanxi Innovative Research Team for Key Science and Technology (No. 2023-CX-TD-46). L.S. acknowledges the financial support from the Shanghai Key Laboratory of Material Frontiers Research in Extreme Environments (MFree), China (No. 22dz2260800) and Shanghai Science and Technology Committee, China (No. 22JC1410300).

Supplementary materials

Supplementary material associated with this article can be found, in the online version, at doi:10.1016/j.actamat.2026.121909.

References

[1] S. Prameela, T.M. Pollock, D. Raabe, M.A. Meyers, A. Aitkaliyeva, K. Chintersingh, Z. Cordero, L. Graham-Brady, Materials for extreme environments, Nat. Rev. Mater. 8 (2023) 81.
[2] V.I. Levitas, High pressure phase transformations revisited, J. Phys.: Condens. Matter. 30 (2018) 163001.
[3] D. Errandonea, Pressure-induced phase transformations, Crystals 10 (2020) 595.
[4] D. Errandonea, Y. Meng, M. Somayazulu, D. Hausermann, Pressure-induced α→ω transition in titanium metal: a systematic study of the effects of uniaxial stress, Physica B 355 (2005) 116–125.
[5] V.I. Levitas, A. Dhar, K. Pandey, Tensorial stress-plastic strain fields in α - ω Zr mixture, transformation kinetics, and friction in diamond-anvil cell, Nat. Commun. 14 (2023) 5955.
[6] B. Straumal, A. Gornakova, G. Davdian, A. Mazilkin, L. Gondek, M. Szczerba, A. Korneva, Review - phase transitions in Ti alloys driven by the high pressure torsion, Mater. Trans. 64 (2023) 1820–1832.
[7] D. Brown, J. Almer, L. Balogh, E. Cerreta, B. Clausen, J. Escobedo-Diaz, T. Sisneros, P. Mosbrucker, E. Tulk, S. Vogel, Stability of the two-phase (α/ω) microstructure of shocked zirconium, Acta Mater 67 (2014) 383–394.
[8] H. Zong, X. Ding, T. Lookman, J. Sun, Twin boundary activated α/ω phase transformation in titanium under shock compression, Acta Mater 115 (2016) 1–9.
[9] L. Li, W. Jia, V. Ji, Effect of laser shock peening on α→ω phase transformation in high-purity titanium, Vacuum 206 (2022) 111510.
[10] E. Cerreta, J. Escobedo, P. Rigg, C. Trujillo, D. Brown, T. Sisneros, B. Clausen, M. F. Lopez, T. Lookman, C. Bronkhorst, F. Addessio, The influence of phase and substructural evolution during dynamic loading on subsequent mechanical properties of zirconium, Acta Mater 61 (2013) 7712–7719.
[11] S. Sikka, Y.K. Vohra, R. Chidambaram, Omega phase in materials, Prog. Mater. Sci. 27 (1982) 245–310.
[12] D. Trinkle, R. Hennig, S. Srinivasan, D. Hatch, M. Jones, H. Stokes, R. Albers, J. Wilkins, New mechanism for the α to ω martensitic transformation in pure titanium, Phys. Rev. Lett. 91 (2003) 025701.
[13] Y.K. Vohra, S. Sikka, S. Vaidya, R. Chidambaram, Impurity effects and reaction kinetics of the pressure-induced α → ω transformation in Ti, J. Phys. Chem. Solids 38 (1977) 1293–1296.
[14] J. Silcock, An X-ray examination of the ω phase in TiV, TiMo and TiCr alloys, Acta Metallurgica 6 (1958) 481–493.
[15] E. Cerreta, G. Gray III, A. Lawson, T. Mason, C. Morris, The influence of oxygen content on the α to ω phase transformation and shock hardening of titanium, J. Appl. Phys. 100 (2006) 013530.
[16] R. Hennig, D. Trinkle, J. Bouchet, S. Srinivasan, R. Albers, J. Wilkins, Impurities block the α to ω martensitic transformation in titanium, Nat. Mater. 4 (2005) 129–133.
[17] Y.K. Vohra, P. Spencer, Novel γ-phase of titanium metal at Megabar pressures, Phys. Rev. Lett. 86 (2001) 3068–3071.
[18] Y. Akahama, H. Kawamura, T. Le Bihan, New δ (Distorted-bcc) titanium to 220 GPa, Phys. Rev. Lett. 87 (2001) 275503.
[19] K. Dang, C. Tome, L. Capolungo, The role of deviatoric stress and dislocations on the α to ω phase transformation in Ti, Acta Mater 244 (2023) 118510.
[20] M. Perez-Prado, A. Gimazov, O. Ruano, M. Kassner, A. Zhilyaev, Bulk nanocrystalline ω-Zr by high-pressure torsion, Scripta Mater 58 (2008) 219–222.
[21] K.K. Pandey, V.I. Levitas, In situ quantitative study of plastic strain-induced phase transformation under high pressure: example for ultra-pure Zr, Acta Mater 196 (2020) 338–346.
[22] V.I. Levitas, High-pressure mechanochemistry: conceptual multiscale theory and interpretation of experiments, Phys. Rev. B 70 (2004) 184118.
[23] M. Arul Kumar, T. Yu, Y. Wang, Z. Jianzhong, R. McCabe, C. Tome, L. Capolungo, Effect of dislocation slip and deformation twinning on the high-pressure phase transformation in Zirconium, Scripta Mater 242 (2024) 115941.
[24] A.H. Zahiri, J. Ombogo, L. Cao, Formation of {11-22} contraction twins in titanium through reversible martensitic phase transformation, Scripta Mater 195 (2021) 113694.
[25] M. Arul Kumar, N. Hilairet, R. McCabe, T. Yu, Y. Wang, I.J. Beyerlein, C. Tome, Role of twinning on the omega-phase transformation and stability in zirconium, Acta Mater 185 (2020) 211–217.
[26] Y. Peng, R. Ji, T. Phan, W. Gao, V.I. Levitas, L. Xiong, An atomistic-to-microscale computational analysis of the dislocation pileup-induced local stresses near an interface in plastically deformed two-phase materials, Acta Mater 226 (2022) 117663.
[27] Y. Peng, R. Ji, T. Phan, L. Capolungo, V.I. Levitas, L. Xiong, Effect of a micro-scale dislocation pileup on the atomic-scale multi-variant phase transformation and twinning, Comput. Mater. Sci. 230 (2023) 112508.
[28] M. Javanbakht, V.I. Levitas, Phase field simulations of plastic strain-induced phase transformations under high pressure and large shear, Phys. Rev. B 94 (2016) 214104.
[29] M. Javanbakht, V.I. Levitas, Nanoscale mechanisms for high-pressure mechanochemistry: a phase field study, J. Mater. Sci. 53 (2018) 13343–13363.
[30] G. Singh, U. Ramamurty, Boron modified titanium alloys, Prog. Mater. Sci. 111 (2020) 100653.
[31] B. Li, C. Hu, K. Shi, D. Pan, X. Zhang, L. Liu, L. Gao, S. Li, Z. Wang, G. Li, Y. Fu, L. Su, S. Li, Pressure-driven structural transformation and lattice deformation in TiB reinforced titanium matrix composites: an in-situ synchrotron x-ray diffraction study, Mater Charact 206 (2023) 113411.
[32] I. Dragomir, T. Ungar, Contrast factors of dislocations in the hexagonal crystal system, J. Appl. Cryst. 35 (2002) 556–564.
[33] T. Ungar, S. Ott, P. Sanders, A. Borbely, J. Weertman, Dislocations, grain size and planar faults in nanostructured copper determined by high resolution x-ray diffraction and a new procedure of peak profile analysis, Acta Mater 46 (1998) 3693–3699.
[34] S.N. Dey, P. Chatterjee, S.Sen Gupta, Dislocation induced line-broadening in cold-worked Pb-Bi binary alloy system in the α-phase using X-ray powder profile analysis, Acta Mater 51 (2003) 4667–4677.
[35] T. Shintani, Y. Murata, Y. Terada, M. Morinaga, Evaluation of dislocation density in a Mg-Al-Mn-Ca alloy determined by X-ray diffractometry and transmission electron microscopy, Mater. Trans. 51 (2010) 1067–1071.
[36] T. Ungar, G. Ribarik, L. Balogh, A.A. Salem, S.L. Semiatin, G.B.M. Vanghan, Burgers vector population, dislocation types and dislocation densities in single grains extracted from a polycrystalline commercial-purity Ti specimen by X-ray line-profile analysis, Scripta Mater 63 (2010) 69–72.
[37] S. Li, Y. Han, X. Wang, G. Huang, M. Fang, H. Shi, J. Le, W. Lu, Novel strategy of planting nano-TiB fibers with ultra-fine network distribution into Ti-composite powder and its thermal transition mechanism, Composites Communications 29 (2022) 101002.
[38] T. Ungar, A. Borbely, The effect of dislocation contrast on x-ray line broadening: A new approach to line profile analysis, Appl. Phys. Lett. 69 (1996) 3173.
[39] Y. Li, M. Huang, A method to calculate the dislocation density of a TWIP steel based on neutron diffraction and synchrotron x-ray diffraction, Acta Metallurgica Sinica 56 (2020) 487–493.
[40] K. Mathis, K. Nyilas, A. Axt, I. Dragomir, T. Ungar, P. Lukac, The evolution of non-basal dislocations as a function of deformation temperature in pure magnesium determined by X-ray diffraction, Acta Mater 52 (2004) 2889.
[41] T. Ungar, O. Castelnau, G. Ribarik, M. Drakopoulos, J. Bechade, T. Chauveau, A. Snigirev, I. Snigireva, C. Schroer, B. Bacroix, Grain to grain slip activity in plastically deformed Zr determined by X-ray micro-diffraction line profile analysis, Acta Mater 55 (2007) 1117.
[42] L. Ming, M. Manghnani, K. Katahara, Phase transformations in the Ti-V system under high pressure up to 25 GPa, Acta Metall 29 (1981) 479–485.
[43] T. Ungar, Microstructural parameters from X-ray diffraction peak broadening, Scripta Mater 51 (2004) 777–781.
[44] B. Li, D. Pan, X. Zhang, L. Liu, L. Gao, S. Li, Y. Qin, Y. Fu, S. Li, Deformation behavior of TiB reinforced Ti and Ti6Al4V composite particles under in-situ microcompression, Mater. Sci. Eng. A 890 (2024) 145903.
[45] J. Yang, W. Deng, Q. Li, X. Li, A. Liang, Y. Su, S. Guan, J. Wang, D. He, Strength enhancement of nanocrystalline tungsten under high pressure, Matter Radiat. Extremes 5 (2020) 058401.
[46] A. Muiruri, M. Maringa, W. Preez, Evaluation of dislocation densities in various microstructures of additively manufactured Ti6Al4V (Eli) by the method of X-ray diffraction, Materials (Basel) 13 (2020) 5355.
[47] H. Alkhazraji, M. Salih, Z. Zhong, M. Mhaede, H. Brokmeier, L. Wagner, N. Schell, Estimation of dislocation density in cold-rolled commercially pure titanium by using synchrotron diffraction, Metall. Mater. Trans. B 45 (2014) 1557–1564.
[48] T. Ungar, M. Glavicic, L. Balogh, K. Nyilas, A. Salem, G. Ribarik, S. Semiatin, The use of X-ray diffraction to determine slip and twinning activity in commercial-purity (CP) titanium, Mater. Sci. Eng. A 493 (2008) 79–85.
[49] I. Dragomir, D. Li, G. Castello-Branco, H. Garmestani, R. Snyder, G. Ribarik, T. Ungar, Evolution of dislocation density and character in hot rolled titanium determined by X-ray diffraction, Mater Charact 55 (2005) 66–74.
[50] J. Gubicza, I. Dragomir, G. Ribarik, S. Baik, Y.T. Zhu, R. Valiev, T. Ungar, Dislocation structure and crystallite size distribution in plastically deformed Ti determined by X-ray peak profile analysis, Z. Metallkde. 94 (2003) 1185.
[51] A. Podolskiy, C. Mangler, E. Schafler, E. Tabachnikova, M. Zehetbauer, Microstructure and mechanical properties of high purity nanostructured titanium processed by high pressure torsion at temperatures 300 and 77 K, J. Mater. Sci. 48 (2013) 4689–4697.
[52] F. Lin, V.I. Levitas, K.K. Pandey, S. Yesudhas, C. ParK, Rules for the crystallite size and dislocation density evolution in phases during α-ω transformation in Zr under high-pressure and severe plastic flow, Acta Mater 295 (2025) 121151.
[53] K.K. Pandey, V.I. Levitas, C. Park, G. Shen, In situ study of microstructure evolution and α → ω phase transition in annealed and pre-deformed Zr under hydrostatic loading, J. Appl. Phys. 136 (2024) 115901.
[54] T.H. Simm, Peak broadening anisotropy and the contrast factor in metal alloys, Crystals 8 (2018) 212.

[55] T.H. Simm, P.J. Withers, J. Quinta da Fonseca, Peak broadening anisotropy in deformed face-centred cubic and hexagonal close-packed alloys, J. Appl. Cryst. 47 (2014) 1535–1551.
[56] A. Pavlenko, A. Dobromyslov, N. Taluts, S. Malyugina, S. Mokrushin, Shock-wave properties and deformation-induced structure of commercial-purity titanium, Phys. Metal. Metallography 122 (2021) 794–799.
[57] Y. Qi, X. Wang, P. Tian, W. Zhuang, Y. Li, Z. Chu, X. Ding, J. Sun, Explosive compression strengthened a near-α titanium alloy with high strength, J. Alloy Compounds 1030 (2025) 180896.
[58] H. Feng, Y. Zhou, D. Jia, Q. Meng, J. Rao, Growth mechanism of In situ TiB whiskers in spark plasma sintered TiB/Ti metal matrix composites, Cryst. Growth Des. 6 (2006) 1626–1630.
[59] T. Sawahata, N. Nishiyama, M. Arita, Y. Kawabata, M. Matsushita, K. Ohara, Y. Higo, F. Wakai, Z. Horita, High compressive strength of bulk polycrystalline ω phase in pure titanium, Mater. Trans. 66 (2025) 616.
[60] L. Su, K. Shi, L. Zhang, Y. Wang, G. Yang, Static and dynamic diamond anvil cell (s-dDAC): A bidirectional remote controlled device for static and dynamic compression/decompression, Matter Radiat. Extremes 7 (2022) 018401.
[61] D. Tomasino, C.S. Yoo, Time-resolved X-ray diffraction of Ti in dynamic-DAC, AIP Conf. Proc. 1793 (2017) 060002.
[62] C. Greeff, D. Trinkle, R. Albers, Shock-induced α–ω transition in titanium, J. Appl. Phys. 90 (2001) 2221–2226.
[63] L. Huston, L. Miyagi, R. Husband, K. Glazyrin, C. Kiessner, M. Wendt, H. Liermann, B. Sturtevant, New dynamic diamond anvil cell for time-resolved radial x-ray diffraction, Rev. Sci. Instrum. 95 (2024) 043904.
[64] Y. Zhao, J. Zhang, Enhancement of yield strength in zirconium metal through high-pressure induced structural phase transition, Appl. Phys. Lett. 91 (2007) 201907.
[65] D. He, T. Duffy, X-ray diffraction study of the static strength of tungsten to 69 GPa, Phys. Rev. B 73 (2006) 134106.
[66] C.J. Boehlert, S. Tamirisakandala, W.A. Curtin, D.B. Miracle, Assessment of in situ TiB whisker tensile strength and optimization of TiB-reinforced titanium alloy design, Scripta Mater 61 (2009) 245–248.
[67] M. Wang, X.Y. Xu, H.Y. Wang, L.H. He, M.X. Huang, Evolution of dislocation and twin densities in a Mg alloy at quasi-static and high strain rates, Acta Mater 201 (2020) 102.
[68] M. Fitzpatrick, P.J. Withers, A. Baczmanski, M. Hutchings, R. Levy, M. Ceretti, A. Lodini, Changes in the misfit stresses in an Al/SiCp metal matrix composite under plastic strain, Acta Mater 50 (2002) 1031.
[69] H. Mughrabi, Dual role of deformation-induced geometrically necessary dislocations with respect to lattice plane misorientations and/or long-range internal stress, Acta Mater 54 (2006) 3417–3427.
[70] K.B. Panda, K.S. Ravi Chandran, First principles determination of elastic constants and chemical bonding of titanium boride (TiB) on the basis of density functional theory, Acta Mater 54 (2006) 1641–1657.
[71] H. Mughrabi, Dislocation wall and cell structures and long-range internal stresses in deformed metal crystals, Acta Metall 31 (1983) 1367–1379.
[72] H. Mughrabi, Deformation-induced long-range internal stresses and lattice plane misorientations and the role of geometrically necessary dislocations, Philos. Mag. 86 (2006) 4037–4054.
[73] Y. Zhu, X. Wu, Heterostructured materials, Prog. Mater. Sci. 131 (2023) 101019.
[74] V.I. Levitas, Continuum mechanical fundamentals of mechanochemistry, High Pressure Surface Science and Engineering, CRC Press, 2003.
[75] H. Zong, T. Lookman, X. Ding, C. Nisoli, D. Brown, S. Niezgoda, J. Sun, The kinetics of the ω to α phase transformation in Zr, Ti: analysis of data from shock-recovered samples and atomistic simulations, Acta Mater 77 (2014) 191–199.
[76] J. Le, Y. Han, J. Xiang, L. Lei, G. Huang, W. Lu, Understanding the role of multi-scale reinforcements on severe plastic deformation of titanium matrix composites, Metall. Mater. Trans. A 51A (2020) 1732.
[77] M.K. Koo, J.S. Park, M.K. Park, K.T. Kim, S.H. Hong, Effect of aspect ratios of in situ formed TiB whiskers on the mechanical properties of TiBw/Ti-6Al-4V composites, Scripta Mater 66 (2012) 487–490.
[78] V.I. Levitas, O.M. Zarechnyy, Kinetics of strain-induced structural changes under high pressure, J. Phys. Chem. B 110 (2006) 16035–16046.
[79] A. Dewaele, V. Stutzmann, J. Bouchet, F. Bottin, F. Occelli, M. Mezouar, High pressure-temperature phase diagram and equation of state of titanium, Phys. Rev. B 91 (2015) 134108.
[80] E.Y. Tonkov, E.G. Ponyatovsky, Phase transformations of elements under high pressure, CRC press, Boca Raton, 2004.
[81] J. Zhang, Y. Zhao, R. Hixson, G. Gray III, L. Wang, W. Utsumi, S. Hiroyuki, H. Takanori, Experimental constraints on the phase diagram of titanium metal, J. Phys. Chem. Solids 69 (2008) 2559–2563.
[82] A. Saxena, T. Taushik, S. Gupta, Shock loading characteristics of Zr and Ti metals using dual beam velocimeter, J. Appl. Phys. 118 (2015) 075904.
[83] N. Velisavljevic, M. Jacobsen, Y.K. Vohra, Structural phase stability in nanocrystalline titanium to 161 GPa, Mater. Res. Express 1 (2014) 035044.